Prestoring Lithium into Stable 3D Nickel Foam Host as Dendrite-Free Lithium Metal Anode

Shang-Sen Chi, Yongchang Liu, Wei-Li Song, Li-Zhen Fan, and Qiang Zhang**

Lithium metal is considered a "Holy Grail" of anode materials for high-energy-density batteries. However, both dendritic lithium deposition and infinity dimension change during long-term cycling have extremely restricted its practical applications for energy storage devices. Here, a thermal infusion strategy for prestoring lithium into a stable nickel foam host is demonstrated and a composite anode is achieved. In comparison with the bare lithium, the composite anode exhibits stable voltage profiles (200 mV at 5.0 mA cm^{-2}) with a small hysteresis beyond 100 cycles in carbonate-based electrolyte, as well as high rate capability, significantly reduced interfacial resistance, and small polarization in a full-cell battery with $Li_4Ti_5O_{12}$ or $LiFePO_4$ as counter electrode. More importantly, in addition to the fact that lithium is successfully confined in the metallic nickel foam host, uniform lithium plating/stripping is achieved with a low dimension change (merely ≈3.1%) and effective inhibition of dendrite formation. The mechanism for uniform lithium stripping/plating behavior is explained based on a surface energy model.

1. Introduction

Metallic lithium (Li), the most ideal anode material for rechargeable batteries, possesses the advantages of lightweight (0.53 g cm^{-3}), a high specific theoretical capacity (3860 mAh g^{-1}), and the lowest electrochemical potential (−3.04 V vs the standard hydrogen electrode).[1–3] However, Li metal anode has been severely impeded from practical applications by the challenges of dendritic Li growth and the infinity dimension change during repeated stripping/plating that give rise to serious potential safety hazards and rapid capacity decay.[4,5] To address these issues, consecutive researches have been devoted to explore the mechanism of Li stripping/plating[6–8] and mitigate dendrite formation along with a relative infinity dimension change.[9–11]

It is well-known that Li reacts spontaneously with most organic electrolyte solvents and Li salt anions due to its highly reactive nature, forming a solid electrolyte interphase (SEI) layer on a Li surface.[12] Meanwhile, Li metal surface is asperous in the scale of micrometers, thus the protuberances possess much higher surface energy than other sites. As shown in Figure S1 (Supporting Information), when Li is plating, the SEI layer is broken, and Li dendrites are generated preferentially at the protuberances sites where both the electrons and the Li ions are locally enhanced.[12–16] Consequently, a large quantity of fresh Li underneath is exposed to the electrolyte, generating new SEI layer. With durative forming and growing of the Li dendrites during repeated cycling, the accompanying large-surface-area of SEI layers induces a constant loss of both working Li metal and electrolyte, leading to a low Coulombic efficiency and a rapid capacity decay. Moreover, Li dendrites are prone to break off and separate from Li metal anode, which is caused by the roots of Li dendrites tendency to easily receive electrons and early dissolution. This results in the formation of dead Li and the rapid capacity decay of a working Li metal anode. The accumulation of dead Li and Li dendrites brings about relative dimension change due to the "hostless" nature of Li, causing tremendous internal stress fluctuations and the floating interface in the batteries. Apart from that, nonhomogeneous Li dendrites easily induce an internal short circuit and a thermal runaway with potential safety hazards. Therefore, suppressing the formation of Li dendrites and alleviating the dimension change during continuous cycling are recognized to be very critical for a full utilization of Li metal anode.

Many strategies have been proposed to regulate the unexpected dendritic Li formation, including exploiting electrolyte additives for SEI stabilization,[17–20] designing high-modulus solid/composite electrolytes to impede dendrite infiltration,[21–29] and engineering stable artificial interfacial layer for dendrite inhibition.[30–33] However, the dramatical electrode dimension change caused by the "hostless" Li plating/stripping at a high areal capacity is a huge challenge. A host with abundant prestoring Li is therefore strongly considered. Various

---

S.-S. Chi, Dr. Y. C. Liu, Prof. W.-L. Song, Prof. L.-Z. Fan
Key Laboratory of New Energy Materials and Technologies
Institute of Advanced Materials and Technology
University of Science and Technology Beijing
Beijing 100083, China
E-mail: fanlizhen@ustb.edu.cn

Prof. Q. Zhang
Beijing Key Laboratory of Green Chemical Reaction Engineering and Technology
Department of Chemical Engineering
Tsinghua University
Beijing 100084, China
E-mail: zhang-qiang@mails.tsinghua.edu.cn

The ORCID identification number(s) for the author(s) of this article can be found under http://dx.doi.org/10.1002/adfm.201700348.

DOI: 10.1002/adfm.201700348

current collector hosts, such as 3D current collectors with a submicron skeleton,[11] 3D porous copper current collector,[34] 3D graphene/metal scaffolds,[35] and free-standing copper nanowire network,[36] have been used to host the Li metal by an electrodeposition approach. In addition, porous graphene/graphite networks[37–39] and conductive nanostructured graphene scaffolds[40] are also used to store Li metal through electroplating. The hosts used in these reports not only provide free space for prestoring metallic Li, receiving Li ions during fabrication, and later continuous cycling, respectively, but also enhance the electrochemical deposition by framework-induced uniform Li plating/stripping. Consequently, minimum dimension change and effective dendrite restraint were achieved. However, the electrodeposition approach for prestoring Li, which is operated via assembling host and bare Li foil into a working cell, generally brings about uneven Li deposition since that most of Li metal prefers to plate on the top part of the host network due to the shorter Li ion diffusion pathway.[36] Moreover, the batteries have to be disassembled and the resultant electrode are further cleaned to remove residual Li salts and electrolyte during electrodeposition of Li metal, which results in tedious materials processing of electrode fabrication and hinders practical applications of composite Li metal anodes. Very recently, Cui's group reported a remarkable thermal infusion strategy for the fabrication of Li metal anodes, which is realized through molten Li infusion into stable hosts, including layered reduced graphene oxide (rGO) with nanoscale interlayer gaps and surface-modified 3D scaffolds with a layer of ZnO or Si.[9–11] Compared with the electrodeposition strategy, the thermal infusion method exhibits prominent advantages of (i) avoidance employ of sacrificing cells, (ii) removal of unstable species by molten Li, and (iii) facile homogeneous and pyknotic Li deposition.[9] Nevertheless, it is a grand challenge to search a rational host for thermal infusion due to the poor wettability of liquefied Li and the instability of host under high temperature environment. A host capable of applying to thermal infusion is strongly expected.

In this contribution, we report the exploration of metallic nickle (Ni) foam as a stable host for prestoring Li via thermal infusion strategy. The resultant Li–Ni composite electrode demonstrates a stable voltage profile with a small hysteresis for more than 100 cycles in a symmetric cell. When assembled into a full-cell battery against $Li_4Ti_5O_{12}$ (LTO) or $LiFePO_4$ (LFP) electrode, Li–Ni composite anode affords superb rate capability, apparently reduced interfacial resistance, and small polarization after 100 cycles. More importantly, effective dendrite inhibition and low dimension change are achieved. The mechanism for uniform Li stripping/plating behavior is also explored.

2. Results and Discussion

Figure 1a illustrates the fabrication procedure of a Li–Ni composite anode. A facile thermal infusion strategy was employed to fabricate a Li–Ni composite. As shown in Movie S1 in the Supporting Information, uniform and rapid Li intake is realized facilely by putting the Ni foam (Figure 1b) on the top of molten Li. The liquefied silvery Li draws into a Ni foam through only 31 s. A Li–Ni composite is achieved (Figure 1c). The areal loading of Li in Li–Ni composite is 26 mg cm^{-2}. The weight percentage of Li in the composite is 50%, and the corresponding gravimetric specific capacity is ≈1932 mAh g^{-1} (Table S1, Supporting Information).

The morphology of a Ni foam (Figure 1d–f) and a Li–Ni composite (Figure 1g–i) were characterized using scanning electron microscopy (SEM). The porous nature of the Ni foam was revealed from the top SEM image (Figure 1d), where large open pores with diameters around 100–800 µm were observed and the Ni framework protuberances marked with yellow arrow appeared on the top. The thickness of the Ni foam was ≈800 µm (Figure 1e). The Ni foam was constructed by continuous 3D Ni backbone with a width of ≈100 µm (Figure 1f). Once molten Li was infused into a Ni foam, the large pores were filled by Li and the Ni framework protuberances were well retained on the top (Figure 1g), indicating architectures of 3D Ni foam were well preserved during the Li thermal infusion. The liquefied Li was spread across the whole Ni foam completely. Figure 1h,i displays the low- and high-magnification cross-sectional SEM images of Li–Ni composite, which exhibited a thickness of ≈800 µm. The surface was asperous with many protuberances. Despite the protuberant structure, the Ni protuberances do not pierce the separator because they are obtuse and bulky.

The X-ray diffraction (XRD) pattern of the Li–Ni composite (Figure S2, Supporting Information) reveals three phases in the composite. The identified peaks are indexed as Ni, Li, and Li_2O_2, confirming that Li metal was stabilized in the Ni foam. The appearance of Li_2O_2 phase is caused by the chemical reaction of Li with oxygen in air during the XRD test.

As an ideal scaffold for Li infusion, Ni foam has several notable merits: (1) The molten Li can wet the metallic Ni foam easily, which is owing to the low surface energy and continuous 3D architectures of Ni foam. Both the high temperature of molten Li metal (≈400 °C) and a facile infusion way (putting Ni foam on the top of molten Li) that can further facilitate high-heat molten Li infusion. This is different from previous reports,[9–11] in which Li metal was infiltrated into nanostructured scaffolds. (2) The superior high melting point (1400 °C) of Ni foam, which is far above the melting point of Li (180 C), ensures that the Ni foam can withstand the high temperature during thermal infusion of molten Li. (3) The porous structure of Ni foam affords a large surface area for Li infusion and Li stripping/plating during fabrication and later repeated cycling, respectively. (4) The superb electronic and ionic conductivity of the interconnected 3D Ni architectures affords unblocked ion/electron pathway, which enables rapid ion/electron transport during Li deposition/dissolution.

To evaluate the electrochemical performance of the Li–Ni composite, symmetrical coin cells (2032-type) with two identical Li–Ni composite were assembled using a carbonate-based electrolyte. Noticeably, it is quite a challenging job using a carbonate-based electrolyte in Li metal batteries because of its comparatively positive reduction potential and the formation of a relatively brittle SEI layer.[41] However, it is very meaningful to probe the Li metal in a carbonate environment since carbonate electrolytes are practically applied for commercial lithium ion batteries.[9] Meanwhile, control cells were fabricated using bare Li foil electrodes, whose weights were equal to that of the Li existing in the Li–Ni composite (Table S1, Supporting

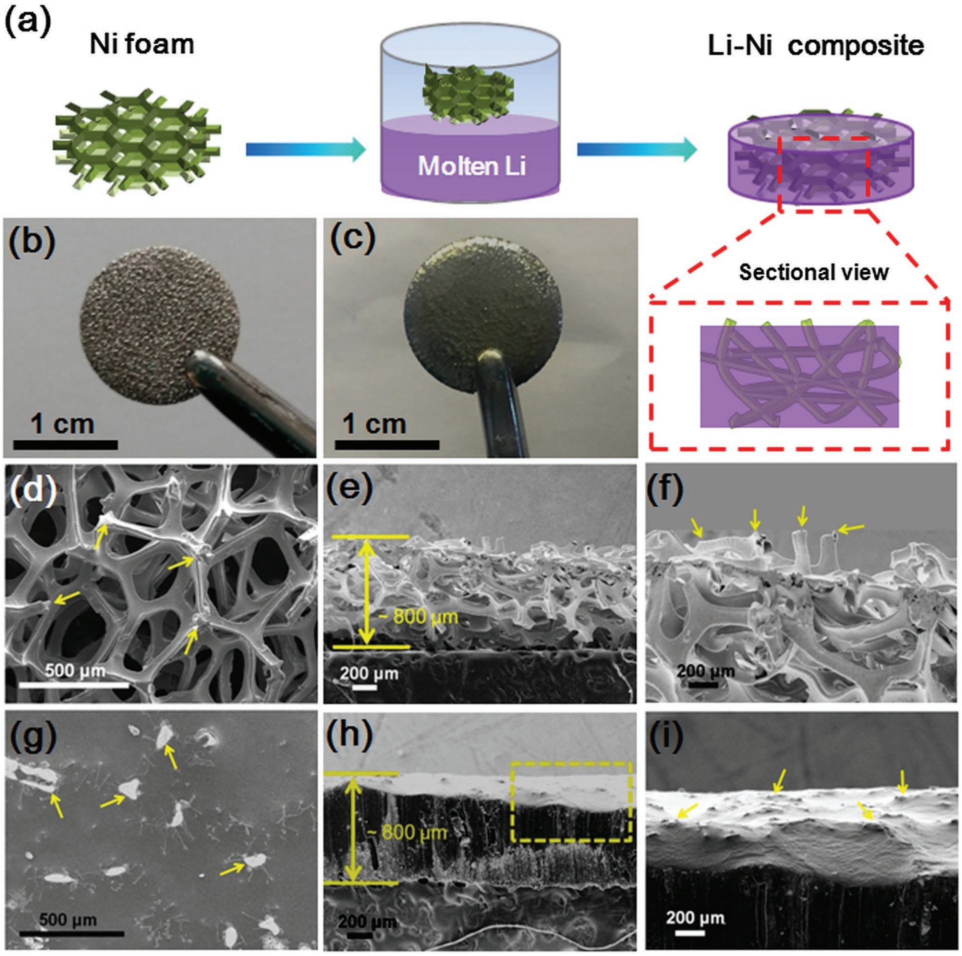

Figure 1. Fabrication of the Li–Ni composite anode. a) Schematic of Li–Ni anode fabrication process. The Ni foam was put on the top of the molten Li. The molten Li steadily infuses into the Ni foam, forming a Li–Ni composite anode. Corresponding digital camera images of b) the Ni foam and c) the Li–Ni composite. SEM images of the d–f) Ni foam and g–i) Li–Ni composite anode.

Information), and were assembled with the same battery thickness by adding a thin steel sheet for standardizing the test (see more details in the Experimental Section).

Figure 2a exhibits the voltage hysteresis of symmetric Li–Ni composite cells and the bare Li foil counterparts for more than 100 cycles at 1.0, 3.0, and 5.0 mA cm^{-2}. The definition of voltage hysteresis is admitted as a sum of overpotential for Li stripping and Li plating.[42] Li–Ni cell exhibited stable voltage profiles with a small hysteresis beyond 100 cycles at 1.0 mA cm^{-2}, whereas the bare Li foil cell displayed a gradual augment in hysteresis, where the overpotential first increases, and then fluctuates. A gradual increase was found in the Li electrode at the 40th cycle, and a sudden voltage drop and conspicuous voltage fluctuation were detected after 68 cycles, which was attributed to unstable property of intrinsic SEI on Li metal anode.[22,42,43] When the cycling capacity was increased to 3 mAh cm^{-2}, the Li–Ni composite cells still exhibited much improved cycling stability (Figure S3, Supporting Information). Additionally, the bare Li symmetrical cell displayed an irregularly and obviously fluctuating voltage at 3.0 mA cm^{-2}, which remained constant throughout the whole cycle. In contrast, the Li–Ni cell not only exhibited a much lower Li stripping/plating overpotential but also attained a stable cycling for more than 100 cycles. When the current density was increased to 5.0 mA cm^{-2}, stable cycling beyond 100 cycles with stable hysteresis can be attained, whereas the Li foil counterparts exhibited gradual hysteresis augment.

Correspondingly, electrochemical impedance spectrum (EIS) measurements were performed on symmetric cells before cycling and after 100 cycles to reveal the mechanism of significantly reduced polarization and very stable cycling of Li–Ni composite anode. As shown in Figure 2b, the SEI interfacial resistance and the Li surface charge transfer impedance are estimated from the semicircle at a high frequency range. A tremendous interfacial resistance (≈250 Ω), which derives from the native SEI layer formed on the Li surface due to its highly reactive nature,[9,13] was discovered in a bare Li symmetric cell before cycling. After 100 cycles, the interfacial resistance decreased to a much lower value (≈45 Ω). This is ascribed to the morphological changes that occurred on the Li surface, where the collapse of SEI layer and the formation of Li dendrites significantly increased the surface area of a working Li metal. However, for the Li–Ni composite cell, the interfacial resistance demonstrated a constantly low value of ≈90 Ω before cycling

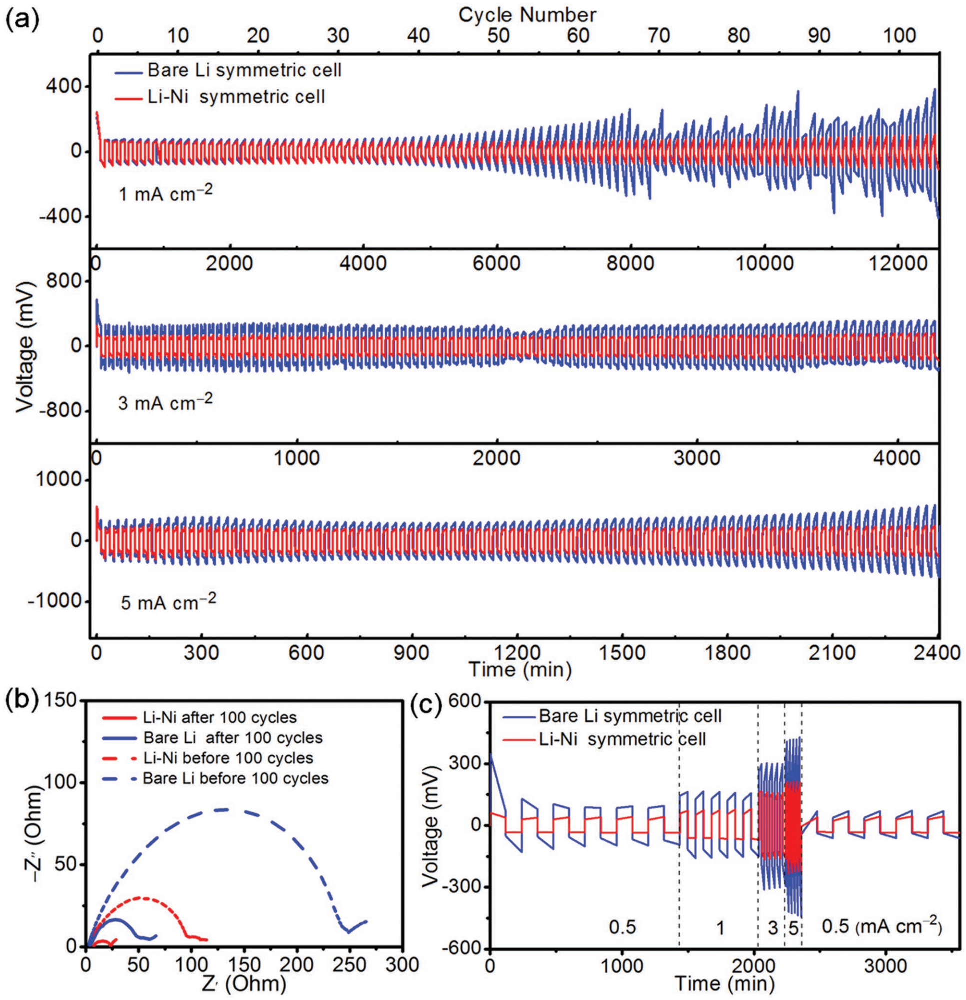

Figure 2. Electrochemical performance of Li–Ni composite electrodes. a) Comparison of the cycling stability of the Li–Ni composite (red) and bare Li electrode (blue) symmetrical cell at a current density of 1, 3, and 5 mA cm^{-2} . b) Nyquist plot of the impedance spectra of the Li–Ni composite and the bare Li cell before/after 100 cycles at a current density of 1 mA cm^{-2}. c) Rate performances of the Li–Ni composite and the bare Li electrode symmetric cells at different current densities.

and ≈25 Ω after 100 cycles. This phenomenon is explained by the much better electrode stability and easier Li stripping/plating kinetics of a Li–Ni composite compared with those of bare Li.

The rate behavior of a symmetrical cell was presented in Figure 2c and Figure S4 (Supporting Information). Li–Ni electrode demonstrated a stable changing voltage polarization of 50, 90, 150, and 200 mV at a current density of 0.5, 1.0, 3.0, and 5.0 mA cm^{-2}, respectively. Nevertheless, a larger voltage hysteresis was observed in the bare Li electrode, especially at a high current density of 5.0 mA cm^{-2}. This phenomenon is attributed to the high specific kinetic obstacle, which inclined to nonuniform Li plating/stripping at large current density.[43–45] The improved rate performance of Li–Ni compared to bare Li electrode exposes favorable electron/ion conductivity, owing to the unimpeded electron/ion transport pathway inside the Li–Ni composite.[46]

To observe the morphology variation of bare Li and Li–Ni composite in a symmetrical cell after cycling, both top and cross-section SEM images were recorded after 10 and 100 cycles at 1.0 mA cm^{-2} with a stripping/plating capacity of 1 mAh cm^{-2}. **Figure 3**a–d exhibits the surface and cross-section of the pristine Li foil, which exhibited a rough surface with plentiful fluctuant sites and a thickness of ≈400 µm. The Li foil surface displayed a more uneven surface with mossy and rugged Li deposition and the thickness increased to ≈420 µm after 10 cycles (Figure S5a–d, Supporting Information). Seriously, rough surface of Li metal with excessive Li dendrites and dead Li with a thickness of ≈490 µm was observed after 100 cycles (Figure 3e–h). On the contrary, the top surface of Li–Ni composites maintained flat without detectable Li dendrites. The Li–Ni electrode is still with a thickness of ≈800 µm after 100 cycles (Figure 3i–l and Figure S5e–h, Supporting Information). The thickness of bare Li foil is different from Li–Ni electrode. This is attributed to the fact that the weight of bare Li foil is equal to that of the Li existing in the Li–Ni composite (Table S1, Supporting Information) for standardizing the test, thereby assembling the same battery thickness by adding a thin steel sheet. Magnified SEM image (Figure 3j) of the Li–Ni electrode after 100 cycles exhibits that the top surface was consistent of

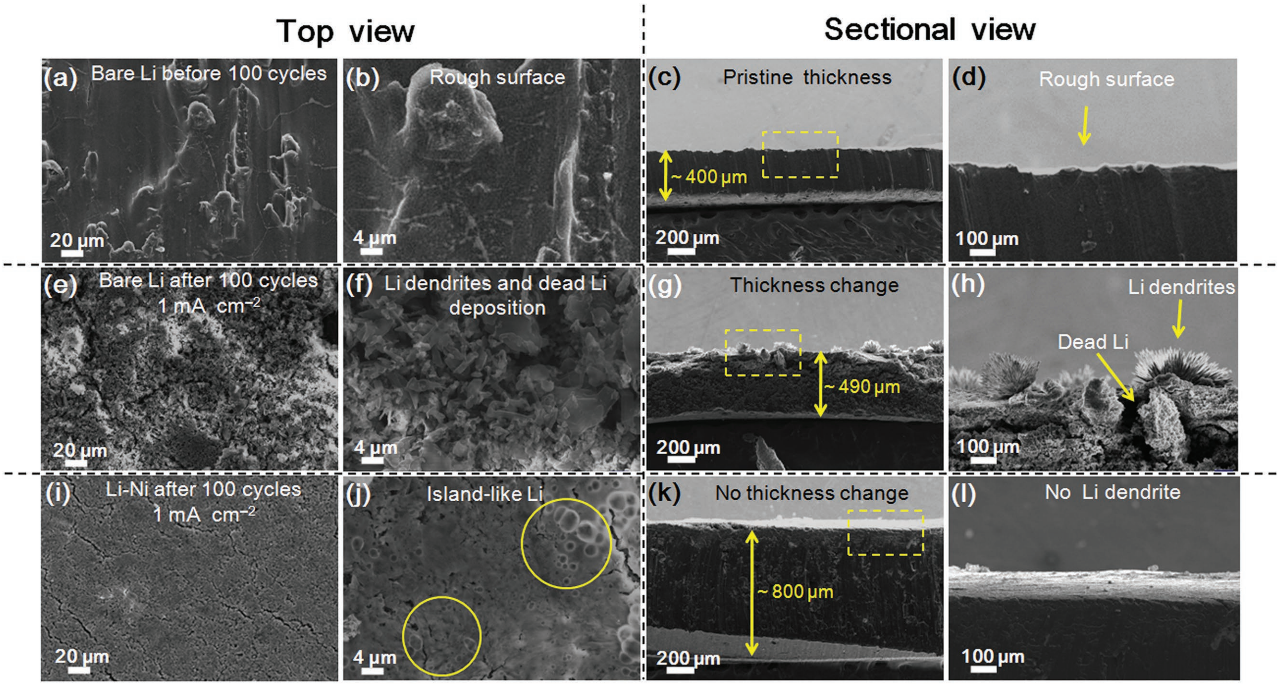

Figure 3. Morphology evolution of the routine Li and Li–Ni composite symmetrical cell after cycling. Surface and cross-section SEM images of the bare Li foil electrodes a–d) before and e–h) after 100 stripping/plating. i–l) Top and cross-section SEM images of the Li–Ni composite electrodes after 100 galvanostatic cycles. The current density was maintained at 1 mA cm^{-2} with a stripping/plating capacity of 1 mAh cm^{-2}.

abundant island-like Li. The surface of the Li metal was covered by a fuzzy thin layer. The energy-dispersive X-ray spectroscopy (EDS) mapping (Figure S6, Supporting Information) revealed that the elements of C, O, F, P (from SEI layer and Li salt), and Ni (from the Ni foam backbone) were nonuniformly distributed on the surface. This is corresponded to the inhomogeneous distribution of the island-like Li covered by a SEI layer. In addition, dendrite-free surface and no thickness change were observed for the Li–Ni composite after 100 cycles at a large current density of 3.0 or 5.0 mA cm^{-2} (Figures S7 and S8, Supporting Information). Only a slight surface crack was detected for the Li–Ni composite, whereas Li foils displayed significant cracks even at a current density of 3.0 mA cm^{-2} (Figure S7a,c,d, Supporting Information). Severe surface shedding was discovered on the surface of cycled Li foil at 5.0 mA cm^{-2} (Figure S8a,c,d, Supporting Information). The surface peeling off is explained by the roots of Li dendrites tendency to receive electrons and early dissolution in a carbonate-based electrolyte (Figures S7b and S8b, Supporting Information), resulting in effective shedding of the accumulation layer of dead Li and Li dendrites. Such completely different variation demonstrates the merit of the Li–Ni composite on Li dendrite inhibition and dimension change alleviation.

Moreover, Li–Ni composites with different thicknesses were fabricated by controlling the contact duration of Ni foam with molten Li (Figure S9, Supporting Information). Interestingly, nonuniform lithium deposition behavior occurs in the Li–Ni composite with the thickness of less than 800 µm (Figure S10, Supporting Information). When the thickness is more than 800 µm, Li dendrites generate on the surface of the Li–Ni composite (Figure S11, Supporting Information), indicating that the optimal thickness of the Li–Ni composite anode is 800 µm in this work.

The Li–Ni composite electrodes were directly paired with LTO (**Figure** 4a–c and Figure S12, Supporting Information) and LFP (Figure 4d and Figure S13, Supporting Information) electrodes. Compared with routine Li metal anode, the Li–Ni anodes consistently exhibited a much better rate capability, lower interfacial resistance, and smaller polarization. A much higher LTO capacity was achieved with Li–Ni composite anodes in the rate plot (Figure 4a). The cell was consecutively cycled at 0.2, 0.5, 1, 2, 4, and 0.2 C (1C = 170 mA g^{-1}) with superior charge capacities of 159, 151, 144, 128, 104, and 156 mAh g^{-1}, respectively. In contrast, bare Li foil cells offer a much lower capacity of 122, 106, and 87 mAh g^{-1} with pronounced instability especially at the high rate of 1, 2, and 4 C, respectively, which is due to a much more instable Li metal anode and an uneven Li deposition/decomposition induced by the high specific kinetic hurdle at high current densities.[43,44] Correspondingly, EIS of the two cells after cycling was also investigated to evaluate the interfacial stability. The interfacial resistance and surface charge transfer resistance of the Li–Ni composite anode (≈60 Ω) is much lower than that of the bare Li anode (≈250 Ω) (Figure 4b). This confirms the Li–Ni anode based cell possesses an extraordinary interfacial stability.

Cyclic voltammetry (CV) has been utilized to evaluate the Li$^+$ diffusion kinetics of electrode materials.[47] Herein, kinetic analysis based on CV analysis was performed for further insight into the electrochemistry variation of the LTO/Li–Ni cell. According to the CV curves in Figure 4c and Figure S12a (Supporting Information), direct comparison of the cathodic and anodic peaks in the two cells exhibits a much narrow and sharp

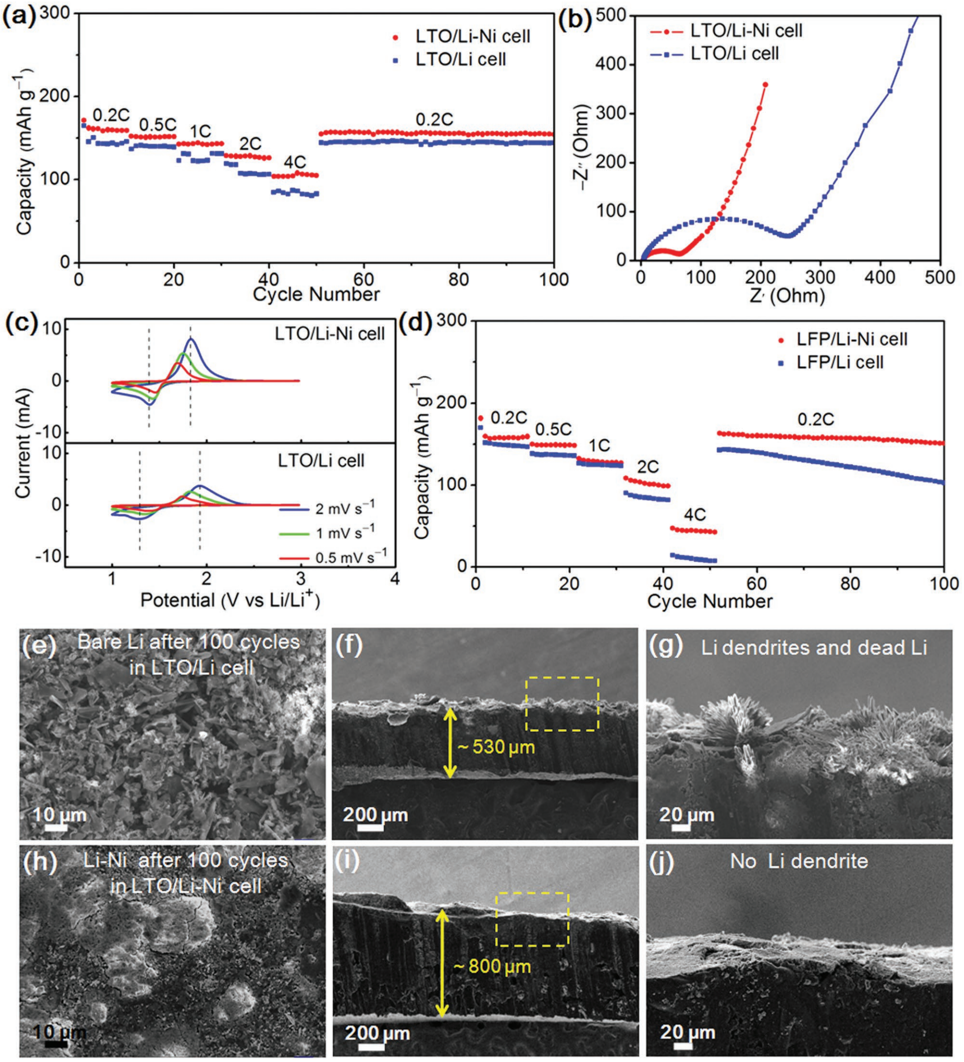

Figure 4. Comparison of the characterization of the Li–Ni composite and the Li paired with LTO and LFP. a) Rate capability of the LTO/Li–Ni and LTO/Li cells at different rates from 0.2 to 4 C (1C = 170 mA g^{-1}). b) Nyquist plots of the full cells as marked after 100 cycles. c) CV curves at various scan rates from 0.5 to 2 mV s^{-1}. d) Rate capability of the LFP/Li–Ni and LFP/Li cells at different rates from 0.2 to 4 C (1C = 170 mA g^{-1}). Surface and cross-section SEM images of e–g) Li and h–j) Li–Ni paired with LTO electrode after 100 cycles at various rates.

state in the Li–Ni cell, demonstrating a much better structural stability (especially the superb stability of anode–electrolyte interfaces) and electrochemical properties in a Li–Ni cell.[48] Meanwhile, it is obvious that the smaller peak separation (the distance of dash line) compared to bare Li cell is displayed at various scan rates ranging from 0.2 to 5 mV s^{-1}, indicating small polarization in the Li–Ni cell.[49] The reduction of polarization in Li–Ni anode is also observed in the voltage profile comparison between LTO/Li–Ni and LTO/Li cells at different rates (Figure S12b–f, Supporting Information). The CV analysis is consistent with the results described in Figure 4a,b. Furthermore, the same phenomenon can be observed using LFP as cathode (Figure 4d and Figure S13, Supporting Information). For evaluating the cycling stability and the Coulombic efficiency of the Li–Ni composite electrode in practical rechargeable Li metal batteries, high areal capacity of LTO was paired with our Li–Ni electrode. As shown in Figure S14 (Supporting Information), the cell with Li–Ni electrode demonstrated a capacity of ≈125 mAh g^{-1} at 100th cycle, which is much higher than the cell with routine Li metal anode with a capacity of about 30 mAh g^{-1}. A Coulombic efficiency of 90% is obtained on the cell with Li–Ni anode, which is also larger than the cell with Li anode (72%, see more details in Note Section in the Supporting Information). This data confirmed the less Li loss on the Li–Ni anode in a working Li metal battery compared with routine Li metal anode.

To reveal the stability of the Li metal anode, the morphology of Li–Ni composite and bare Li after 100 cycles at various current rates was collected. The surface of cycled bare Li electrode exhibits an uneven surface with excessive Li dendrites (Figure 4e), whereas the cross-section of cycled Li exhibits an increased thickness of ≈530 µm. The interface between electrode and separator is rough and loose, which is composed of Li dendrites and dead Li (Figure 4f,g). In contrast, no dendrite formation and thickness variation were found on cycled Li–Ni composite electrode (Figure 4h–j). The Li–Ni composite can accommodate the volume change during repeated Li stripping/plating, thus contributing to steady electrode structure and interface in a working cell.

The stripping/plating behavior of the Li–Ni composite was further investigated using a two-electrode symmetric cell at 1 mA cm^{-2} (**Figure 5** and Figure S15, Supporting Information). After stripping away 5 mAh cm^{-2} Li (Figure 5a and Figure S15a, Supporting Information), top Li around Ni backbones was dissolved preferentially and Ni skeletons were partially exposed on the surface of Li–Ni composite. This indicated that the stripping reaction primarily occurred on the surface site of Ni skeletons. The irregular flake-like Li around exposed Ni skeletons was observed, which was explained by the nonuniform stress distribution on surface. When 10 mAh cm^{-2} Li was stripped, top Ni skeleton with dark Li particles and massive flake-like Li appeared on the surface (Figure 5b and Figure S15b, Supporting Information). With the stripping capacity increasing to 20 mAh cm^{-2}, top intact Ni skeleton with dark Li particles and massive flake-like Li were observed (Figure 5c and Figure S15c, Supporting Information). Subsequently, Li was primarily deposited on the surface of Ni skeletons when 15 mAh cm^{-2} Li was plated. The Li metal was partially filled in the space between the skeletons, forming an uneven surface. Denser and thicker Li was detected on Ni skeletons surface (Figure 5d and Figure S15d, Supporting Information). In this situation, direct Li nucleation on the Ni skeletons surface was easier owing to the high-activity of Li particles with several sub-micrometer in diameter, as reported in the previous studies[11,49] and illustrated by the SEM image (inset in Figure S15c, Supporting Information). This afforded beneficial sites for Li growth while producing inhomogeneous morphology. Finally, after all stripped Li (20 mAh cm^{-2}) was plated back, the top Ni skeleton, again, was overlaid with Li and no dendrite can be detected (Figure 5e and Figure S15e,f, Supporting Information).

Synchronously, the thickness variation of the Li–Ni composite at different capacities of Li stripping/plating was investigated by cross-section SEM images. As shown in Figure 5f–h, the thickness of the Li–Ni composite gradually decreased from 750 to 600 µm with the variation of the stripping capacity from 5 to 20 mAh cm^{-2}. When the capacity of Li plating increased from 15 to 20 mAh cm^{-2}, the thickness restored to ≈800 µm (Figure 5i,j), corresponding to the original thickness of Li–Ni composite. From the Figure 5f–j, the variation thickness of Li–Ni composite was 50, 100, 200, 150, and 200 µm, corresponding to 5, 10, 20, 15, and 20 mAh cm^{-2} capacity of Li stripping or plating, respectively. Therefore, 1 mAh cm^{-2} capacity represents ≈10 µm thickness change in the Li–Ni composite. In addition, according to theoretical calculation of the thickness variation for Li–Ni electrode (Method Section, Supporting Information), the calculated value of 1 mAh cm^{-2} capacity represents ≈9.69 µm thickness change. As a result, the Li–Ni composite electrode thickness fluctuation is calculated for merely ≈3.1%. Even after repetitive 100 cycles, as demonstrated by the previous SEM image (Figure 3k), the change in thickness is minimal. On the contrary, the thickness fluctuation is tremendous for bare Li foil (Figure 3g). Consequently, the Ni foam host is essential to mitigate the volume change of Li metal anode, addressing the potential security issue caused by the "hostless" Li plating/stripping.

For further understanding the Li stripping/plating behavior of Li–Ni composite, magnified cross-section SEM images, as well as the proposed mechanism based on the surface energy model,[50] are illustrated in Figures 5k–o and 6, respectively. According to the surface energy model, high surface energy guided the generation of highly concentrated

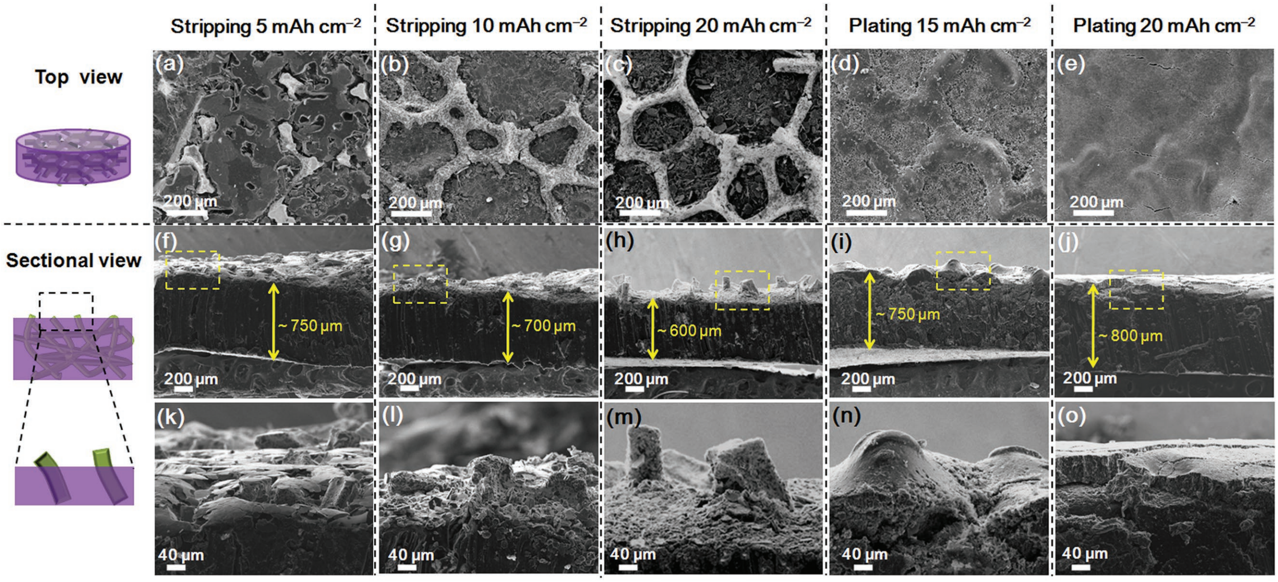

Figure 5. Morphology variation of the Li–Ni composite with different amounts of Li plating/stripping. Surface and cross-sectional SEM images of the Li–Ni composite with a Li stripping of a,f,k) 5, b,g,l) 10, and c,h,m) 20 mAh cm^{-2}, then plating of d,i,n) 15 mAh cm^{-2} and e,j,o) 20 mAh cm^{-2}. The current density was 1 mA cm^{-2}.

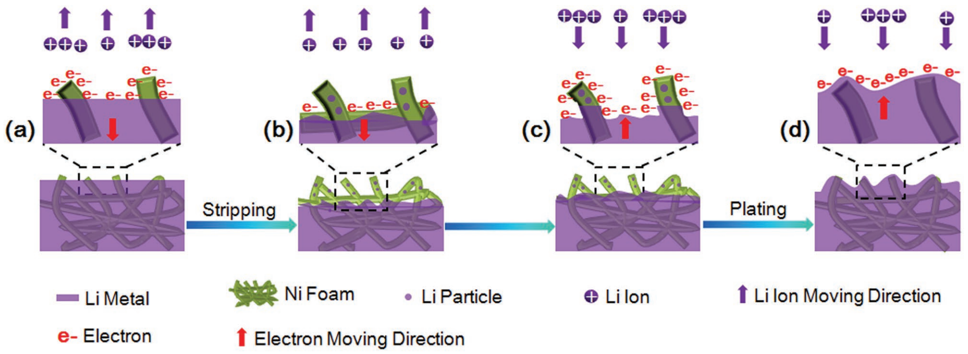

Figure 6. Schematic illustration of the Li stripping/plating behavior occurred on the surface of Li–Ni composite anode with different amounts of Li stripping/plating.

electron/ion on the sites with large specific surface area during stripping/plating process. The morphology evolution shown in Figure 5k–m can be explained rationally by the highly concentrated electron/ion in the stripping process. This occurred on the surface of Ni framework protuberances in the first place (**Figure 6**a), and then appeared on the salient Li metal surface. Ultimately, it showed up at the interface between Li–Ni composite and electrolyte (Figure 6b). Reversibly, the observed Li deposition in Figure S16 (Supporting Information) and Figure 5n–o indicates that the electrons/ions intensively gather on the surface of Ni skeleton during plating of Li metal (Figure 6c) and then on the space between the salient Li metal surfaces (Figure 6d). This achieves a dendrite-free surface that is made up of many sizes of Li islands. The Ni foam host not only can capture molten lithium via a thermal infusion strategy, but also accommodate the surface energy between the lithium anode and electrolyte during repeated Li stripping/plating. The accommodation of Li metal into a 3D conductive host is very effective for confined volume change and suppression of Li dendrites.

Our work demonstrates that Li–Ni composite anode can be fabricated by infusing molten Li into a metallic Ni foam host. The resultant anode has following distinguished advantages for the practical applications of Li metal: (1) Simple manufacturing process: The facile thermal infusion strategy was utilized to obtain Li–Ni composite, avoiding complicated electrodeposition approach that is operated via assembling and disassembling a Li–host cell. The as-obtained Li–Ni composite can be directly applied to the battery system. (2) Improved electrochemistry performance: The Li–Ni composite anode in symmetrical cells exhibits stable voltage profiles with a small hysteresis beyond 100 cycles even at a high current density (5 mA cm^{-2}). Moreover, when assembled into a full-cell battery using LTO or LFP electrode, the Li–Ni anode affords superb rate capability, reduced interfacial resistance, and smaller polarization after 100 cycles compared with routine Li metal anodes. (3) Reduced safety hazards: The low electrode dimension change and dendrite-free deposition are achieved since that the Li metal is effectively confined in the Ni foam host, which accommodate the surface energy of Li–Ni composite anode in the electrochemical cycling, therefore enhancing safety performance of Li metal batteries with Li–Ni composite anode.

3. Conclusions

The metallic Ni foam is employed as a stable host for prestoring Li via a thermal infusion strategy to form a dendrite-free Li–Ni composite anode. The anode exhibits enhanced cycling stability with a low hysteresis for more than 100 cycles even at a very high current density of 5 mA cm^{-2} in carbonate-based electrolyte. Compared with routine pure Li metal anode, a full-cell battery with Li–Ni anode and LTO/LFP cathode exhibits better rate capability, lower interfacial resistance, and smaller polarization. Furthermore, the anode demonstrates a low electrode dimensional change and dendrite-free behavior after 100 cycles both in both symmetric-cell and full-cell systems. Based on the analysis of Li stripping/plating behavior of Li–Ni composite, the Ni foam host not only acts as a caged entrapment for lithium metal, but also accommodates the surface energy of the Li–Ni composite anode during electrochemical cycling, thus preventing dendritic growth of Li metal and restricting dimensional variation of Li electrode (≈3.1%). This work provides an alternative option for the fabrication of safe Li metal anodes, which is of great significance for the practical applications of Li metal anodes in high-energy-density batteries.

4. Experimental Section

Fabrication of Li–Ni Composite Electrodes: Ni foam (99.9% purity) was cut into 1.538 cm^{-2} (diameter of 1.4 cm) disks by a punch machine. In a typical procedure, Ni foam disks were cleaned by performing consecutive ultrasonication in acetone, ethanol, and deionized water for 10 min and finally dried in a vacuum oven. The Li melt-infusion was carried out in an argon-filled glove box with less than 0.1 ppm oxygen and 0.1 ppm H_2O. Li foil (99.9%, Alfa Aesar) was scraped and polished with a sharp blade until the surface of the Li foil was extremely shiny. After polishing, freshly scraped Li foil was put into a stainless-steel crucible and then heated to ≈400 °C on a hotplate. Subsequently, the Ni foam disk was put on the top of the molten Li. Molten Li can steadily climb up and wet the whole Ni foam disk, forming the final Li electrode (Movie S1, Supporting Information). The disk acted as the Li–Ni composite electrode once cooled down to room temperature.

Characterizations: Field-emission SEM images and EDS mappings were obtained on a ZEISS SUPRA 55 microscope. Noticeably, before observing the morphology of the cycled electrodes, the batteries were first disassembled in the glovebox and then gently rinsed with dimethyl carbonate to remove residual Li salts and electrolyte. To observe the cross-section images of the Li metal, the samples were cut in half using a sharp scissor. XRD patterns were recorded on a Rigaku/mac diffractometer with Cu Kα radiation ($\lambda = 0.154$ nm).

Electrochemical Measurements: To probe the electrochemical behavior of Li stripping and plating, the electrodes were assembled into standard 2032-type coin cells in a symmetric cell configuration. The electrodes used herein were either Li–Ni composite electrodes or Li metal foils (99.9%, Alfa Aesar). To fabricate LTO and LFP electrodes for the full-cell battery testing, the active materials (LTO and LFP powders) were mixed with carbon black and polyvinylidene fluoride at a weight ratio of 8:1:1 with *N*-methyl-2-pyrrolidone as the solvent. The particle size distribution of LFP and LTO is 50–800 nm, and the amount of carbon coating in LFP and LTO electrodes is 10%. Electrodes with areal mass loading of 3.0 mg cm^{-2} were used for both LTO and LFP electrodes. For battery cycling with a high amount of Li, LTO electrodes with areal capacities of 6.36 mAh cm^{-2} were used. Celgard 2400 was utilized as the separator. The electrolyte employed was 1.0 M lithium hexafluorophosphate ($LiPF_6$) in a mixture of ethylene carbonate, dimethyl carbonate, and ethyl methyl carbonate (volume ratio of 1:1:1). The dosage of electrolyte in every full cell was 30 µL. Particularly, the weight of routine Li foil iwa equal to that of the Li existing in the Li–Ni composite (Table S1, Supporting Information) for standardizing the test. To guarantee the battery with the same thickness, a thin steel sheet was introduced into bare Li foil electrode. Galvanostatic cycling was conducted on the battery test system (LAND CT2001A, Wuhan JinnuoElectronics, Ltd.). All cells were assembled in an argon-filled glovebox using the same separator and electrolyte. CV and EIS were carried out on an electrochemical workstation (CHI660C, Shanghai Chenhua). The CV was performed at various scan rates from 0.2 to 5 mV s^{-1}. EIS measurements were recorded over the frequency ranging from 100 kHz to 0.01 Hz.

Supporting Information

Supporting Information is available from the Wiley Online Library or from the author.

Acknowledgements

S.-S.C. and Y.C.L. contributed equally to this work. Financial supports from NSF key project of China (51532002), National Basic Research Program of China (2015CB932500), and NSF of China (51372022, 51575030, and 21676160) are gratefully acknowledged.

Conflict of Interest

The authors declare no conflict of interest.

Keywords

batteries, lithium dendrites, lithium metal anodes, nickel foam hosts, surface energy, thermal infusion

Received: January 20, 2017
Revised: March 4, 2017

---

[1] H. Kim, G. Jeong, Y. U. Kim, J. H. Kim, C. M. Park, H. J. Sohn, *Chem. Soc. Rev.* **2013**, *42*, 9011.
[2] W. Xu, J. L. Wang, F. Ding, X. L. Chen, E. Nasybutin, Y. H. Zhang, J. G. Zhang, *Energy Environ. Sci.* **2014**, *7*, 513.
[3] R. G. Cao, W. Xu, D. P. Lv, J. Xiao, J. G. Zhang, *Adv. Energy Mater.* **2015**, *5*, 1402273.
[4] K. Zhang, G. H. Lee, M. Park, W. J. Li, Y. M. Kang, *Adv. Energy Mater.* **2016**, *6*, 1600811.
[5] Q. Q. Liu, C. Y. Du, B. Shen, P. J. Zuo, X. Q. Cheng, Y. L. Ma, G. P. Yin, Y. Z. Gao, *RSC Adv.* **2016**, *6*, 88683.
[6] D. Aurbach, Y. Gofer, J. Langzam, *J. Electrochem. Soc.* **1989**, *136*, 3198.
[7] P. Bai, J. Li, F. R. Brushett, M. Z. Bazant, *Energy Environ. Sci.* **2016**, *9*, 3221.
[8] Y. S. Cohen, Y. Cohen, D. Aurbach, *J. Phys. Chem. B* **2000**, *104*, 12282.
[9] D. Lin, Y. Liu, Z. Liang, H.-W. Lee, J. Sun, H. Wang, K. Yan, J. Xie, Y. Cui, *Nat. Nanotechnol.* **2016**, *11*, 626.
[10] Y. Y. Liu, D. C. Lin, Z. Liang, J. Zhao, K. Yan, Y. Cui, *Nat. Commun.* **2016**, *7*, 10992.
[11] C.-P. Yang, Y.-X. Yin, S.-F. Zhang, N.-W. Li, Y.-G. Guo, *Nat. Commun.* **2015**, *6*, 8058.
[12] X.-B. Cheng, R. Zhang, C.-Z. Zhao, F. Wei, J.-G. Zhang, Q. Zhang, *Adv. Sci.* **2015**, *3*, 1500213.
[13] N.-W. Li, Y.-X. Yin, C.-P. Yang, Y.-G. Guo, *Adv. Mater.* **2016**, *28*, 1504526.
[14] C. M. Park, J. H. Kim, H. Kim, H. J. Sohn, *Chem. Soc. Rev.* **2010**, *39*, 3115.
[15] K. Xu, *Chem. Rev.* **2014**, *114*, 11503.
[16] Y. H. Zhang, J. F. Qian, W. Xu, S. M. Russell, X. L. Chen, E. Nasybulin, P. Bhattacharya, M. H. Engelhard, D. H. Mei, R. G. Cao, F. Ding, A. V. Cresce, K. Xu, J. G. Zhang, *Nano Lett.* **2014**, *14*, 6889.
[17] F. Ding, W. Xu, G. L. Graff, J. Zhang, M. L. Sushko, X. Chen, Y. Shao, M. H. Engelhard, Z. Nie, J. Xiao, X. Liu, P. V. Sushko, J. Liu, J.-G. Zhang, *J. Am. Chem. Soc.* **2013**, *135*, 4450.
[18] H. Ota, K. Shima, M. Ue, J. Yamaki, *Electrochim. Acta* **2004**, *49*, 565.
[19] J. Qian, W. A. Henderson, W. Xu, P. Bhattacharya, M. Engelhard, O. Borodin, J. G. Zhang, *Nat. Commun.* **2015**, *6*, 6362.
[20] X. Q. Zhang, X. B. Cheng, X. Chen, C. Yan, Q. Zhang, *Adv. Funct. Mater.* **2017**, *27*, 1605989.
[21] S. Choudhury, R. Mangal, A. Agrawal, L. A. Archer, *Nat. Commun.* **2015**, *6*, 10101.
[22] Y. Lu, Z. Tu, L. A. Archer, *Nat. Mater.* **2014**, *13*, 961.
[23] Y. Y. Lu, M. Tikekar, R. Mohanty, K. Hendrickson, L. Ma, L. A. Archer, *Adv. Energy Mater.* **2015**, *5*, 1402073.
[24] D. Zhou, R. L. Liu, Y. B. He, F. Y. Li, M. Liu, B. H. Li, Q. H. Yang, Q. Cai, F. Y. Kang, *Adv. Energy Mater.* **2016**, *6*, 1502214.
[25] X.-B. Cheng, T.-Z. Hou, R. Zhang, H.-J. Peng, C.-Z. Zhao, J.-Q. Huang, Q. Zhang, *Adv. Mater.* **2016**, *28*, 2888.
[26] C.-Z. Zhao, X.-B. Cheng, R. Zhang, H.-J. Peng, J.-Q. Huang, R. Ran, Z.-H. Huang, F. Wei, Q. Zhang, *Energy Storage Mater.* **2016**, *3*, 77.
[27] W. Luo, Y. H. Gong, Y. Z. Zhu, K. K. Fu, J. Q. Dai, S. D. Lacey, C. W. Wang, B. Y. Liu, X. G. Han, Y. F. Mo, E. D. Wachsman, L. B. Hu, *J. Am. Chem. Soc.* **2016**, *138*, 12258.
[28] X.-X. Zeng, Y.-X. Yin, N.-W. Li, W.-C. Du, Y.-G. Guo, L.-J. Wan, *J. Am. Chem. Soc.* **2016**, *138*, 15825.
[29] W. Zhou, S. Wang, Y. Li, S. Xin, A. Manthiram, J. B. Goodenough, *J. Am. Chem. Soc.* **2016**, *138*, 9385.
[30] M. H. Ryou, D. J. Lee, J. N. Lee, Y. M. Lee, J. K. Park, J. W. Choi, *Adv. Energy Mater.* **2012**, *2*, 645.
[31] K. Yan, H. W. Lee, T. Gao, G. Y. Zheng, H. B. Yao, H. T. Wang, Z. D. Lu, Y. Zhou, Z. Liang, Z. F. Liu, S. Chu, Y. Cui, *Nano Lett.* **2014**, *14*, 6016.
[32] G. Y. Zheng, S. W. Lee, Z. Liang, H. W. Lee, K. Yan, H. B. Yao, H. T. Wang, W. Y. Li, S. Chu, Y. Cui, *Nat. Nanotechnol.* **2014**, *9*, 618.
[33] Q.-C. Liu, J.-J. Xu, S. Yuan, Z.-W. Chang, D. Xu, Y.-B. Yin, L. Li, H.-X. Zhong, Y.-S. Jiang, J.-M. Yan, X.-B. Zhang, *Adv. Mater.* **2015**, *27*, 5241.

[34] Q. B. Yun, Y. B. He, W. Lv, Y. Zhao, B. H. Li, F. Y. Kang, Q. H. Yang, *Adv. Mater.* **2016**, *28*, 6932.
[35] K. Xie, W. Wei, K. Yuan, W. Lu, M. Guo, Z. Li, Q. Song, X. Liu, J.-G. Wang, C. Shen, *ACS Appl. Mater. Interfaces* **2016**, *8*, 26091.
[36] L. L. Lu, J. Ge, J. N. Yang, S. M. Chen, H. B. Yao, F. Zhou, S. H. Yu, *Nano Lett.* **2016**, *16*, 4431.
[37] R. Mukherjee, A. V. Thomas, D. Datta, E. Singh, J. W. Li, O. Eksik, V. B. Shenoy, N. Koratkar, *Nat. Commun.* **2014**, *5*, 3710.
[38] X.-B. Cheng, H.-J. Peng, J.-Q. Huang, R. Zhang, C.-Z. Zhao, Q. Zhang, *ACS Nano* **2015**, *9*, 6373.
[39] Y. Sun, G. Zheng, Z. W. Seh, N. Liu, S. Wang, J. Sun, H. R. Lee, Y. Cui, *Chem* **2016**, *1*, 287.
[40] R. Zhang, X.-B. Cheng, C.-Z. Zhao, H.-J. Peng, J.-L. Shi, J.-Q. Huang, J. Wang, F. Wei, Q. Zhang, *Adv. Mater.* **2016**, *28*, 1504117.
[41] J. G. Zhang, W. Xu, W. A. Henderson, *Lithium Metal Anodes and Rechargeable Lithium Metal Batteries, Springer Series in Materials Science*, **2017**, vol. *249*.
[42] Z. Liang, D. C. Lin, J. Zhao, Z. D. Lu, Y. Y. Liu, C. Liu, Y. Y. Lu, H. T. Wang, K. Yan, X. Y. Tao, Y. Cui, *Proc. Natl. Acad. Sci. USA* **2016**, *113*, 2862.
[43] G. Bieker, M. Winter, P. Bieker, *Phys. Chem. Chem. Phys.* **2015**, *17*, 8670.
[44] J. Heine, S. Kruger, C. Hartnig, U. Wietelmann, M. Winter, P. Bieker, *Adv. Energy Mater.* **2014**, *4*, 1300815.
[45] N.-W. Li, Y.-X. Yin, J.-Y. Li, C.-H. Zhang, Y.-G. Guo, *Adv. Sci.* **2017**, *4*, 1600400.
[46] H. K. Kang, S. G. Woo, J. H. Kim, S. R. Lee, Y. J. Kim, *Electrochim. Acta* **2015**, *176*, 172.
[47] V. Augustyn, J. Come, M. A. Lowe, J. W. Kim, P. L. Taberna, S. H. Tolbert, H. D. Abruna, P. Simon, B. Dunn, *Nat. Mater.* **2013**, *12*, 518.
[48] F. Wu, G. Q. Tan, R. J. Chen, L. Li, J. Xiang, Y. L. Zheng, *Adv. Mater.* **2011**, *23*, 5081.
[49] S. Z. Xiong, K. Xie, Y. Diao, X. B. Hong, *J. Power Sources* **2013**, *236*, 181.
[50] D. Wang, W. Zhang, W. Zheng, X. Cui, T. Rojo, Q. Zhang, *Adv. Sci.* **2017**, *4*, 1600168.